Astrocytes amplify cerebral blood flow elevation to sustained cortical activation in the awake mouse

Adam Institoris[1], Milène Vandal[4], Govind Peringod[1], Cam Ha Tran[1,3], Xinzhu Yu[2], Cheryl Breiteneder[1], Leonardo Molina[4], Baljit S. Khakh[2], Minh Dang Nguyen[4], Roger J. Thompson[5], Grant R. Gordon[1]*

1) Hotchkiss Brain Institute, Department of Physiology and Pharmacology, Cumming School of Medicine, University of Calgary, Calgary, Alberta, T2N 4N1, Canada
2) Department of Physiology, David Geffen School of Medicine, University of California, Los Angeles, Los Angeles, CA 90095-1751, USA; Department of Neurobiology, David Geffen School of Medicine, University of California, Los Angeles, Los Angeles, CA 90095-1751, USA.
3) Department of Physiology and Cell Biology, Reno School of Medicine, University of Nevada, Reno, NV 89557-352, USA.
4) Hotchkiss Brain Institute, Department of Clinical Neuroscience, Cumming School of Medicine, University of Calgary, Calgary, Alberta, T2N 4N1, Canada
5) Hotchkiss Brain Institute, Department of Cell Biology and Anatomy, Cumming School of Medicine, University of Calgary, Calgary, Alberta, T2N 4N1, Canada

*Corresponding Author / Lead Contact:

Grant R. Gordon

gordong@ucalgary.ca

Room 1B40A, Building HRIC

3330 Hospital Dr. NW

Calgary, AB, Canada

T2N 4N1

Summary

Brain metabolism requires increased local cerebral blood flow (CBF) during neuronal activation to match O_2 supply with demand. This phenomenon, termed functional hyperemia, is also the basis of functional neuroimaging. Ca^{2+} elevation in astrocytes can drive arteriole dilation to increase CBF, yet affirmative necessity and sufficiency evidence under realistic conditions *in vivo* for astrocytes in functional hyperemia is lacking. In awake mice we show that functional hyperemia is bi-phasic and arteriole dilation progresses as sensory stimulation is sustained. Reduction of astrocyte Ca^{2+} signaling *in vivo* reduces sustained but not brief sensory-evoked arteriole dilation. Chemogenetic activation of astrocytes selectively augments sustained hyperemia. NMDA-receptors and epoxyeicosatrienoic acid explain the astrocyte-mediated effects on the late, escalating phase of functional hyperemia but have no impact on brief blood flow events. We propose that a fundamental role of astrocyte Ca^{2+} is to amplify functional hyperemia when neuronal activation is prolonged.

Keywords: neurovascular coupling, astrocyte, functional hyperemia, fMRI, BOLD, NMDA, EETs, Gq-DREADD, calcium clamp, awake *in vivo*

Introduction

Neuronal function requires tight and uninterrupted access to O_2 and glucose via the blood supply because neurons have neither sufficient energy stores nor capacity for anaerobic metabolism. Thus, neural processing of sensory, motor, and cognitive information drive increased regional cerebral blood flow (CBF) for seconds to minutes as needed. This phenomenon – functional hyperemia – is essential for brain metabolism and also serves as the basis of the blood oxygen level-dependent (BOLD) signal of functional magnetic resonance imaging (fMRI)(He et al., 2018; Mateo et al., 2017).

Astrocytes respond to neural activity and their peri-vascular processes/endfeet can release Ca^{2+} dependent messengers to regulate vascular diameter, both *ex vivo* (reviewed in (Howarth, 2014; Mishra, 2017)) and *in vivo* (Masamoto et al., 2015; Takata et al., 2018). However, controversies about the role of astrocytes in functional hyperemia have arisen from challenges in achieving selective activation (Takano et al., 2006), no effect of manipulating astrocyte IP3 signaling (Bonder and McCarthy, 2014; Jego et al., 2014; Nizar et al., 2013; Takata et al., 2013) and side effects of anesthesia/sedation (Thrane et al., 2012; Tran and Gordon, 2015). It remains possible that astrocytes contribute to functional hyperemia only under distinct durations of neural activity and thus requirements for O_2. Increased neural activity is the main driver (Lee et al., 2010) and user of fresh O_2 (Howarth et al., 2012), yet the well-established linear correlation of BOLD signal to neural activity is lost with sustained brain activation (Kahn et al., 2011; Logothetis et al., 2001). Delayed astrocyte Ca^{2+} signals (>3s) to prolonged stimulation may explain amplified CBF responses (Gu et al., 2018; Schulz et al., 2012) and be important for O_2 to reach vulnerable micro-regions of tissue farthest from a blood vessel (Polesskaya et al., 2012). So far, no causal, astrocyte-specific 'necessity' and 'sufficiency' experiments have linked astrocyte Ca^{2+} to functional hyperemia in the awake state, despite correlational studies (Gu et al., 2018; Lind et al., 2018; Otsu et al., 2015; Schulz et al., 2012; Stobart et al., 2018). The model of astrocyte Ca^{2+} in functional hyperemia requires new support, otherwise the framework for local CBF control needs revision.

Using 2-photon fluorescence imaging in awake mice and tools to selectively clamp or augment astrocyte Ca^{2+} *in vivo*, we discovered that astrocyte Ca^{2+} is causal for functional hyperemia only during sustained bouts of sensory activation. Importantly, sustained functional hyperemia is vulnerable because impairments occur in attention deficit (Weber et al., 2005), age-related cognitive impairment (Rombouts et al., 2005), dementia (Rombouts et al., 2007) and stroke (Pineiro et al., 2002). Our findings help clarify neuro-glio-metabolic coupling and provide insight into conditions involving the cerebral microcirculation.

Results

Sustained functional hyperemia escalates and is associated with astrocyte Ca^{2+} transients

Functional hyperemia occurs, in part, by large diameter changes in penetrating arterioles (Chow et al., 2020; Hill et al., 2015; Rungta et al., 2018). Under anesthesia, arteriole/CBF responses to sustained sensory stimulation consist of an initial rise followed by a plateau at close to the same amplitude (Lacroix et al., 2015; Lecrux et al., 2011; Liu et al., 2008; Peng et al., 2002; Toth et al., 2015), while astrocyte Ca^{2+} transients are suppressed (Thrane et al., 2012). Work in awake animals shows arteriole/CBF kinetics are instead biphasic (Drew et al., 2011; Takuwa et al., 2013), but we know little about the mechanisms underlying the early and late phase. We investigated the temporal dynamics of penetrating arteriole diameter and astrocyte Ca^{2+} during brief (5sec) and sustained (30sec) whisker stimulation using 2-photon microscopy in the barrel cortex of awake mice (Fig. 1A). First, imaging through thinned skull of c57bl/6 mice, arteriole responses to whisker stimulation with air puff elicited rapid arteriole dilation that peaked within the first 5sec of stimulation, followed by progressively increasing diameter only when stimulation was maintained for 30sec (t-test P=0.004, Trial (T)= 17, PA=6, N=3; Fig 1B). Arteriole responses were similar in mice with skull and dura removed (N=5)(P=0.64, Two-way ANOVA; Suppl. Fig. 1). Astrocyte endfeet (labelled with Rhod-2/AM) had Ca^{2+} signals that increased after the onset of vasodilation, which remained elevated during stimulation (Fig. 1C). To additionally resolve astrocyte arbor Ca^{2+} dynamics we repeated our experiments in *Aldh1l1*-Cre/ERT2 x RCL-GCaMP6s mice (N=9). We found similar arteriole response dynamics and delayed elevation in Ca^{2+} within endfeet and processes (Fig. 1D), with corresponding onset latencies (One way ANOVA P=0.0001, Fig. 1E) (Tran et al., 2018). Interestingly, peak dilations to 1sec ($\Delta d/d$=6.07±1.2%) and 5sec stimulation ($\Delta d/d$=8.3±1.1%) were not different, but dilation to 30sec stimulation ($\Delta d/d$=25.95±5.7%) was significantly higher due to the putative secondary phase (Friedman-test P=0.001, T=16-24, PA=7, N=6; Fig. 1F). In further support of a biphasic arteriole response, imaging vascular smooth muscle cell Ca^{2+} changes in *PDGFRß*-Cre x RCL-GCaMP6s (T=30, PA=30, N=11) mice during 30sec whisker stimulation showed two separate peaks of Ca^{2+} drop at ~2.5s and between 20-30s (Fig. 1G,H). This suggests separate processes mediate smooth muscle relaxation in the early and late phase of functional hyperemia.

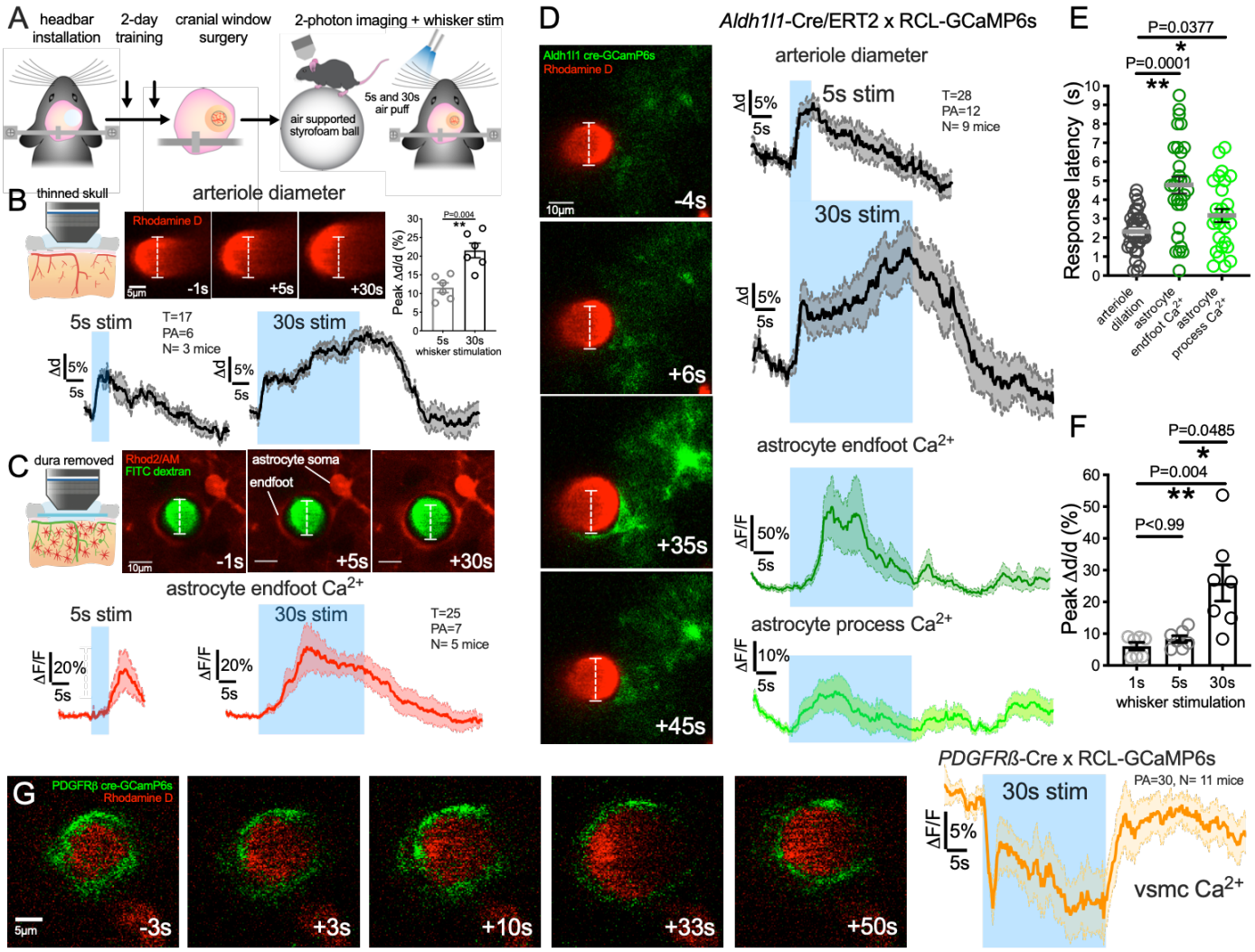
A
headbar installation
2-day training
cranial window surgery
2-photon imaging + whisker stim
air supported styrofoam ball
5s and 30s air puff
B
thinned skull
arteriole diameter
Rhodamine D
-1s
+5s
+30s
5μm
P=0.004
**
Peak Δd/d (%)
5s
30s
whisker stimulation
5s stim
T=17
PA=6
N= 3 mice
30s stim
Δd
5%
5s
C
dura removed
Rhod2/AM
FITC dextran
astrocyte soma
endfoot
10μm
astrocyte endfoot Ca2+
T=25
PA=7
N= 5 mice
ΔF/F
20%
D
Aldh1l1 cre-GCamP6s
Rhodamine D
-4s
+6s
+35s
+45s
Aldh1l1-Cre/ERT2 x RCL-GCaMP6s
arteriole diameter
T=28
PA=12
N= 9 mice
astrocyte endfoot Ca2+
50%
astrocyte process Ca2+
10%
E
P=0.0377
*
P=0.0001
**
Response latency (s)
arteriole dilation
astrocyte endfoot Ca2+
astrocyte process Ca2+
F
P=0.0485
*
P=0.004
**
P<0.99
Peak Δd/d (%)
1s
5s
30s
whisker stimulation
G
PDGFRβ cre-GCamP6s
Rhodamine D
-3s
+3s
+10s
+33s
+50s
PDGFRß-Cre x RCL-GCaMP6s
PA=30, N= 11 mice
vsmc Ca2+

Figure 1. Sustained functional hyperemia escalates and is associated with astrocyte Ca^{2+} transients

A) Cartoon and timeline of the awake mouse 2-photon imaging experiment in barrel cortex.

B) Thinned skull preparation. Time series images (top) showing dilation of a Rhodamine-B-dextran labelled penetrating arteriole in response to whisker stimulation at 5sec and 30sec. Time stamps refer to stimulation onset as 0s. Traces of arteriole dilation (black) to 5 and 30sec whisker stimulation (lower). Summary data of peak diameter changes (top right).

C) Skull/dura removal preparation. Time series images (top) of a Rhod-2 labelled astrocyte around a FITC-dextran labelled penetrating arteriole. Astrocyte Ca^{2+} traces (red) to 5 and 30sec whisker stimulation (bottom).

D) Same as *B* and *C* but in astrocyte *Aldh1l1*-CreERT2 x RCL-GCaMP6s mice. Vasculature labelled with Rhod-B-dextran. Penetrating arteriole (black), endfoot (dark green), astrocyte arbor (light green.

E) Summary of response onset (calculated from each trial as 3 x SD above baseline) for dilation and astrocyte Ca^{2+}.

F) Summary data of peak arteriole dilation to 1, 5 and 30sec stimulation.

G) Time series images of GCaMP6s expressing vascular smooth muscle cells (VSMC) within a penetrating arteriole, and a VSCM Ca^{2+} trace during 30sec whisker stimulation. All trace data show the average with SEM.

153 **Clamping astrocyte Ca^{2+} reduces the late phase of functional hyperemia**

154 Given the stronger association between astrocyte process/endfoot Ca^{2+} and sustained functional
155 hyperemia, and the appearance of a distinct late component in smooth muscle Ca^{2+} traces, we tested for
156 a causal role of astrocyte Ca^{2+} primarily in the late phase of functional hyperemia in awake mice. Previous
157 attempts to connect astrocyte Ca^{2+} to functional hyperemia focused on IP3R2 knockout (Bonder and
158 McCarthy, 2014; Nizar et al., 2013; Takata et al., 2013), but to our knowledge there have been no *in vivo*
159 manipulations to clamp astrocyte Ca^{2+} more generally for CBF control; thereby affecting multiple Ca^{2+}
160 dependent pathways. We made use of the astrocyte Ca^{2+} silencing tool CalEx (Yu et al., 2018). Here,
161 astrocyte-selective AAV (AAV2/5-gfaABC$_1$D-CalEx-mCherry) delivers a high-affinity Ca^{2+} pump to the
162 plasma membrane (Fig. 2A), which reduces evoked and spontaneous elevations in free Ca^{2+} both *in vitro*
163 and *in vivo* (Yu et al., 2018). We validated this tool in our awake animal preparation by comparing
164 astrocyte AAVs for CalEx and GCaMP6f vs control AAVs (AAV2/5-gfaABC$_1$D-tdTomato + GCaMP6f), and
165 examined startle evoked astrocyte Ca^{2+} signals in the barrel cortex (untrained body air puff). Astrocytes
166 expressing CalEx showed markedly reduced startle evoked Ca^{2+} transients (Suppl. Fig. 2). *Post hoc*
167 CalEx expression was confirmed by immunostaining against the reporter mCherry (Fig. 2D).

168 In response to 5sec whisker stimulation, we found that astrocyte CalEx had no impact on evoked
169 arteriole dilation (peak Δd/d: 8.9±0.8%) compared to control AAV (peak Δd/d: 8.7±0.6%, P=0.73, Fig. 2E).
170 Yet remarkably, astrocytic CalEx was effective at reducing arteriole dilation to 30sec whisker stimulation
171 (peak Δd/d: 9.9±1.2%) compared to control (peak Δd/d: 16.9±2%, Fig. 2E) (P_{CalEx}=0.0083, Tukey's test:
172 P=0.0012; 80 trials, PA=16 CalEx, PA=17 control, N=8; mean±SEM) (see Fig. 2E for area under the
173 curve (AUC) data). Again, peak arteriole dilation evoked by 30sec stimulation was larger than 5sec in
174 control mice, due to a progressively increasing late component during sustained activation (P_{StimT}=0.0004;
175 Tukey's test: P<0.0001). Consistent with an action of CalEx primarily on the late component of functional
176 hyperemia, peak arteriole responses to 5 and 30sec stimulation in the CalEx group were similar to control
177 arterioles to 5 sec stimulation (Fig. 2E). These results could not be explained by differences in baseline
178 arteriole tone caused by CalEx expression (Suppl. Fig. 3), and instead suggest that astrocyte Ca^{2+} is
179 important for amplifying arteriole dilation during sustained, but not brief, functional hyperemia.

180 Confirming a clamp on astrocyte Ca^{2+}, CalEx reduced the delayed astrocyte endfoot Ca^{2+} signal
181 caused by 5sec (Fig. 2F) and 30sec stimulation (20±3% (T=45) vs. 44±7% (T=46) mean±SEM), with an
182 overall significance of P_{CalEx}<0.0001 (Fig. 2F). CalEx also diminished astrocyte process Ca^{2+} transient
183 peaks when stimulation was on for 5sec (Fig. 2G) and for 30sec (11±1% (T=46) vs 26±3% (T=45),
184 P_{CalEx}<0.0001, Fig. 2G) (see Fig. 2F,G for AUC data). These data demonstrate that CalEx is an effective
185 tool for clamping astrocyte Ca^{2+} signals *in vivo*.
186 Astrocyte Ca^{2+} transients mediate activity-dependent capillary but not arteriole dilation to 5sec
187 stimulation in acute cortical brain slices (Mishra et al., 2016). Thus, we tested for a causal relationship
188 between long (30sec) but not short (5sec) stimulation-evoked astrocyte Ca^{2+} and penetrating arteriole
189 dilation *ex vivo*, by whole-cell patch infusing the Ca^{2+} chelator BAPTA (10mM) into a network of peri-
190 arteriolar astrocytes. We clamped intracellular free Ca^{2+} close to the resting concentration in astrocytes
191 (~100nM) (Henneberger et al., 2010; Zheng et al., 2015). We allowed 15 mins for the internal solution to
192 equilibrate in the astrocyte network (Rosenegger et al., 2015) and for arteriole tone to stabilize. Rhod-
193 2/AM was used to label large astrocyte and neuronal compartments, as well as the neuropil. Before
194 patching an astrocyte, 30sec of high frequency electrical stimulation elicited Ca^{2+} transients in neurons,
195 the neuropil, astrocyte somata and endfeet, as well as caused arteriole dilation (N=8) (Suppl. Fig. 4). This
196 was then repeated when the astrocyte network was filled with either control internal or Ca^{2+} clamp internal
197 solution. We found that only the Ca^{2+} clamp solution reduced arteriole dilation to 30sec afferent
198 stimulation (N=5, P=0.039). While the astrocyte network filling itself caused reductions in evoked Ca^{2+}
199 from all cell compartments, comparing to the Ca^{2+} clamp solution revealed that the only effect to explain
200 the loss of dilation was the clamp on astrocyte Ca^{2+} (P=0.029, Suppl Fig 4). Importantly, neither clamping
201 astrocyte Ca^{2+}, nor the control patch, affected arteriole dilation to 5sec stimulation, and patching itself (in
202 any condition) did not affect baseline arteriole tone after whole-cell equilibration (Suppl. Fig. 5). These
203 data show that longer neural stimulation is required to recruit Ca^{2+} dependent astrocyte contributions to
204 arteriole dilation in neocortical brain slices.
205
206
207

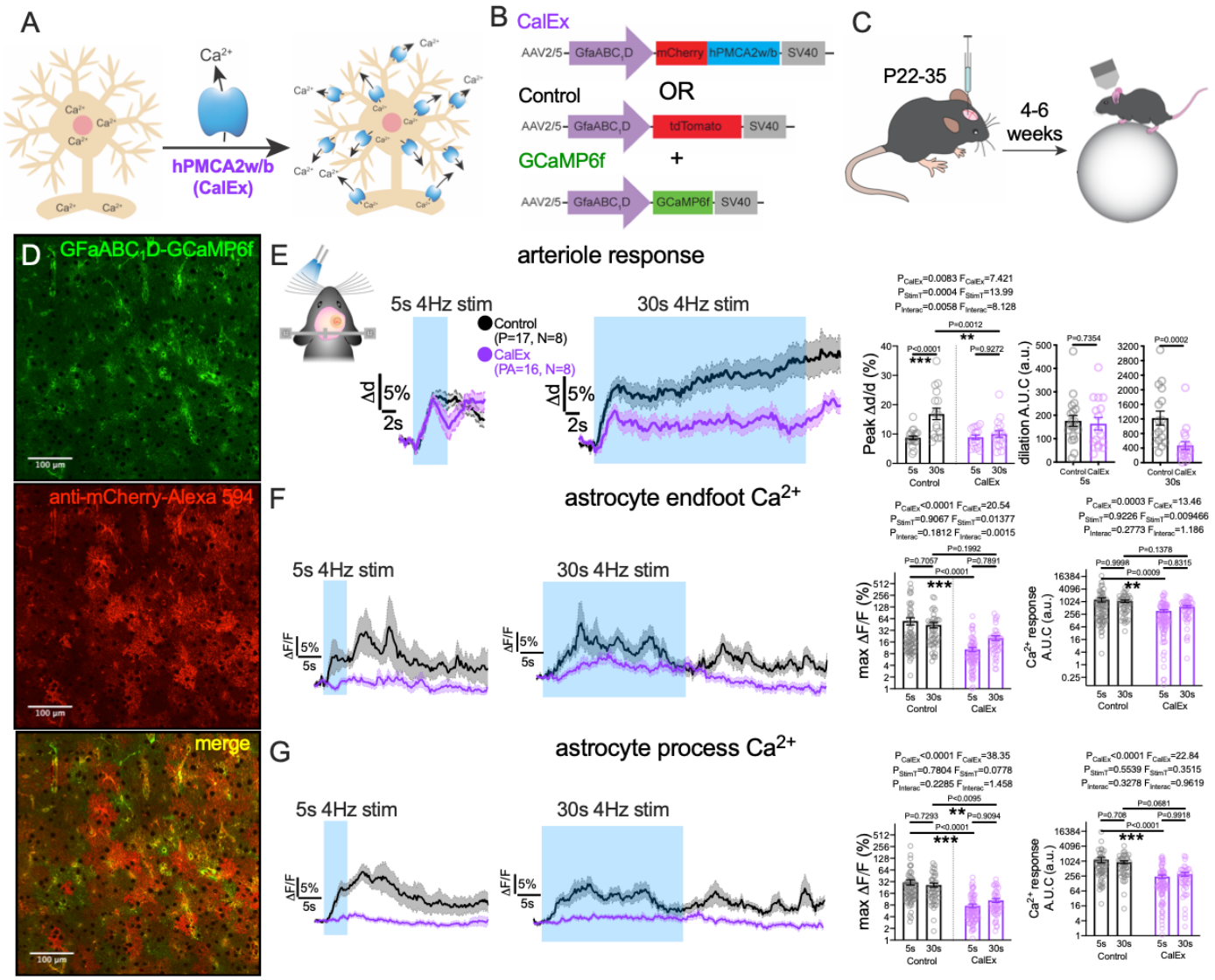
A
Ca2+
hPMCA2w/b
(CalEx)
B
CalEx
AAV2/5
GfaABC1D
mCherry
hPMCA2w/b
SV40
Control
OR
tdTomato
GCaMP6f
+
GCaMP6f
C
P22-35
4-6
weeks
D
GFaABC1D-GCaMP6f
anti-mCherry-Alexa 594
merge
100 µm
E
arteriole response
5s 4Hz stim
30s 4Hz stim
Control
(P=17, N=8)
CalEx
(PA=16, N=8)
Δd
5%
2s
Peak Δd/d (%)
dilation A.U.C (a.u.)
Control
CalEx
F
astrocyte endfoot Ca2+
ΔF/F
5%
5s
max ΔF/F (%)
Ca2+ response A.U.C (a.u.)
G
astrocyte process Ca2+

Figure 2. Clamping astrocyte Ca^{2+} reduces the late phase of functional hyperemia

A) Cartoon of astrocyte Ca^{2+} extrusion tool: a high-affinity plasma membrane Ca^{2+} ATPase hPMCA2w/b (CalEX).

B) Viral vector strategy to express CalEx in astrocyte (or control virus) plus GCaMP6f.

C) Timeline (4-6 weeks) from viral vector intracortical injection to the acute imaging experiment.

D) *Post hoc* immunofluorescence of CalEx expression against the fused mCherry reporter.

E) *Left*: cartoon of awake mouse imaging experiment with whisker stimulation. *Middle*: average arteriole diameter traces with SEM in CalEx and control for 5sec and 30sec whisker stimulation. *Right*: summary data showing peak dilation and area under the curve (AUC) in the four conditions.

F) *Left*: Summary time series data of astrocyte endfoot Ca^{2+} in CalEx vs control for both 5sec and 30sec whisker stimulation. *Right*: Summary of peak and AUC data in the four conditions.

G) Same as *F* but for astrocyte arbor Ca^{2+}.

Chemogenetic activation of astrocytes enhances only the late phase of functional hyperemia

Large astrocyte Ca^{2+} signals occur when synaptic glutamate stimulates Gq-coupled receptors through inositol triphosphate (IP3) signaling (Porter and McCarthy, 1996; Wang et al., 2006; Zonta et al., 2003). However, functional hyperemia is intact in anesthetized/sedated mice lacking IP3-receptor 2 (Bonder and McCarthy, 2014; Jego et al., 2014; Nizar et al., 2013; Takata et al., 2013), the predominant subtype in astrocytes. Nevertheless, the Gq pathway permits manipulation of cytosolic astrocyte Ca^{2+} using chemogenetics, allowing us to explore their contribution in awake mice. We aimed to test if 1) Gq-DREADD activation in astrocytes directly affects arteriole diameter, and if 2) continuous activation of astrocytic Gq either occludes or amplifies functional hyperemia to short vs long whisker stimulation. We crossed *Aldh1l1*-Cre/ERT2 with CAG-LSL-Gq-DREADD (N=6) mice to selectively express hM3Dq receptors on astrocytes, which was confirmed by visualizing the fusion reporter mCitrine (Fig. 3A). A perforated coverglass was applied to the brain surface to permit stable imaging while allowing topical superfusion of the DREADD agonist compound 21 (C21, 10μM). C21 triggered a prolonged (20-40 min) astrocyte soma Ca^{2+} ($\Delta F/F$=63±7%, P<0.0001) and endfoot Ca^{2+} elevation ($\Delta F/F$=34±4%, P=0.0002), accompanied by transient arteriole dilation ($\Delta d/d$=19±2%, P<0.0001)(Fig. 3B,C). After an hour of continuous C21, astrocyte Ca^{2+} levels and arteriole diameter returned to baseline (Fig. 3D). Notably, arteriole dilation to 5sec whisker stimulation remained unchanged in the presence of C21 (peak $\Delta d/d$=12.2±1%) compared to pre-drug control (peak $\Delta d/d$=10.2±1%, P=0.0533, Fig. 3E), whereas 30sec stimulation showed a significant augmentation in only the later phase of functional hyperemia in C21 ($\Delta d/d$=24.7±2.3%), relative to before drug ($\Delta d/d$=17.5±1.9%, P=0.0056, PA=16, N=6 mice, Fig. 3F) (See Fig. 3E,F for AUC data). Our results demonstrate that selectively driving the astrocyte Gq-pathway causes arteriole dilation and only influences the late phase of sustained functional hyperemia.

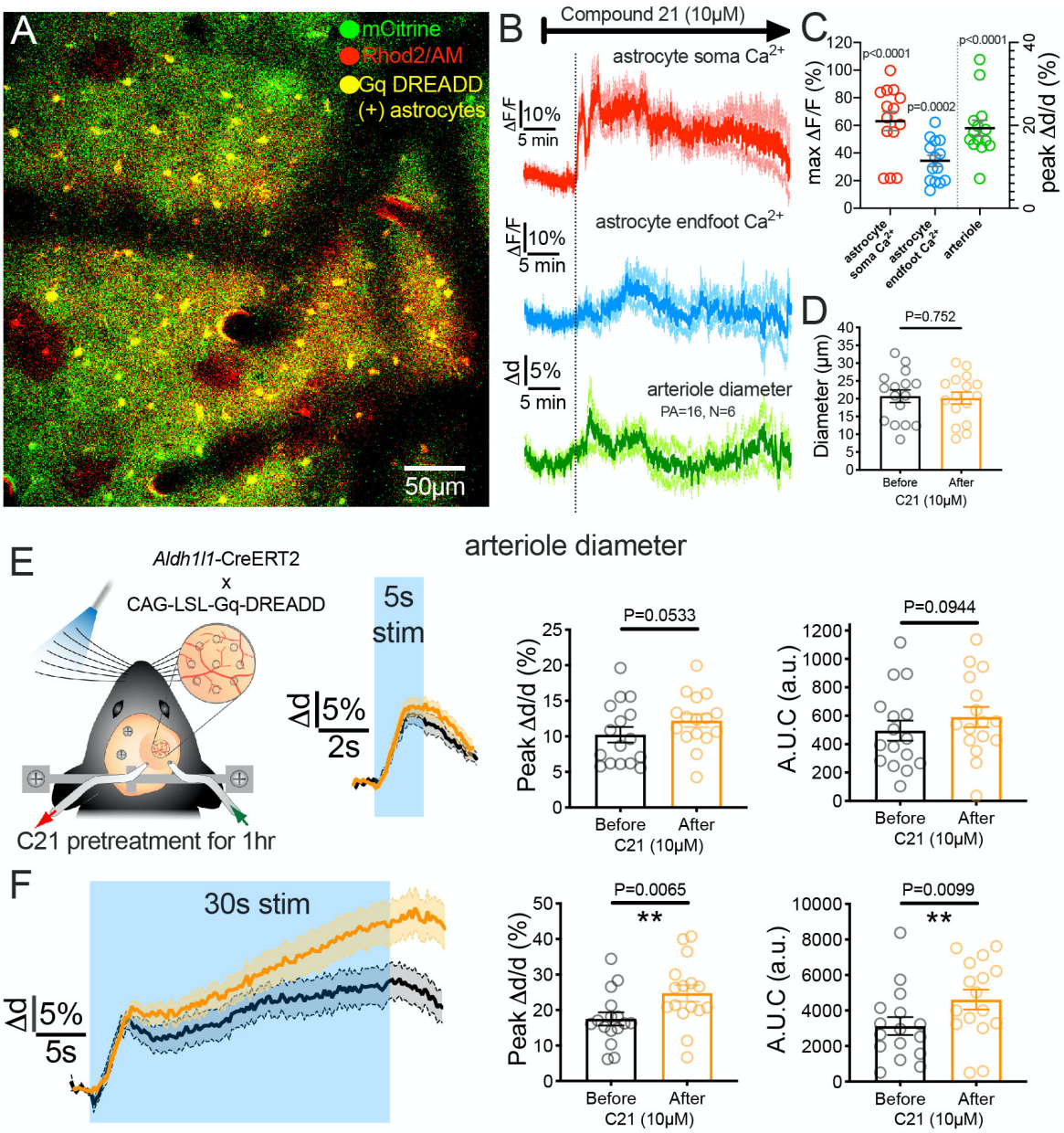
A
mCitrine
Rhod2/AM
Gq DREADD
(+) astrocytes
50μm
B
Compound 21 (10μM)
astrocyte soma Ca2+
ΔF/F
10%
5 min
astrocyte endfoot Ca2+
ΔF/F
10%
5 min
Δd
5%
5 min
arteriole diameter
PA=16, N=6
C
p<0.0001
p=0.0002
p<0.0001
max ΔF/F (%)
peak Δd/d (%)
astrocyte soma Ca2+
astrocyte endfoot Ca2+
arteriole
D
P=0.752
Diameter (μm)
Before
After
C21 (10μM)
E
Aldh1l1-CreERT2
x
CAG-LSL-Gq-DREADD
C21 pretreatment for 1hr
5s
stim
Δd
5%
2s
arteriole diameter
P=0.0533
Peak Δd/d (%)
Before
After
C21 (10μM)
P=0.0944
A.U.C (a.u.)
Before
After
C21 (10μM)
F
30s stim
Δd
5%
5s
P=0.0065
**
Peak Δd/d (%)
Before
After
C21 (10μM)
P=0.0099
**
A.U.C (a.u.)
Before
After
C21 (10μM)

Figure 3. Chemogenetic activation of astrocytes enhances only the late phase of functional hyperemia

A) 2-photon image in barrel cortex of a *Aldh1l1*-Cre x CAG-LSL-Gq-DREADD mouse. Astrocytes are loaded with Rhod-2/AM and express Gq-DREADD-mCitrine.

B) Time series measurements of astrocyte Ca^{2+} and arteriole diameter in response to the local superfusion of the DREADD agonist C21 into the perforated window.

C) Summary data of peak responses in *B*.

D) Summary data showing that in the continual presence of C21 arteriole diameter returns to baseline after 1hr.

E) *Left*: Cartoon of awake mouse sensory stimulation experiment in the presence of C21 delivered via a perforated window. *Middle*: Average arteriole diameter traces with SEM in pre-drug control (black) and in the presence of C21 (orange), in response to 5sec whisker stimulation. *Right*: summary data showing peak dilation and AUC for 5sec in control and C21.

F) Same as *E* but for 30sec whisker stimulation.

320 **NMDA receptors and EETs explain astrocyte-mediated amplification of sustained functional**
321 **hyperemia**
322 N-methyl-D-aspartate (NMDA) receptors are key participants in functional hyperemia. In the canonical
323 model, synapses generate nitric oxide, which causes rapid vasodilation (reviewed in (Busija et al., 2007;
324 Cauli and Hamel, 2010; Hosford and Gourine, 2019)). More recent work implicates NMDA receptors on
325 astrocytes (Mehina et al., 2017) and endothelium (Hogan-Cann et al., 2019) in CBF control, but little is
326 known about the contribution of NMDA receptors to different durations of functional hyperemia in awake
327 animals. As NMDA receptors localize to the cell surface, we used *Aldh1l1*-Cre/ERT2 x R26-Lck-GCaMP6f
328 mice (Fig. 4A,B) to express a plasma membrane-tethered GCaMP6 in astrocytes and imaged endfeet
329 and fine processes surrounding a penetrating arteriole or a precapillary sphincter – a recently identified
330 control point for capillary access to blood (Grubb et al., 2020). We again applied short (5sec) and long
331 (30sec) duration whisker stimulation before and during topical NMDA receptor antagonist D,L-AP5 (1mM)
332 via perforated coverglass. The lck-GCaMP6f showed similar astrocyte Ca^{2+} responses to the cytosolic
333 GCaMP6s under control conditions (*see Fig. 1D*). Notably, in response to 5sec and 30sec whisker
334 stimulation, D,L-AP5 eliminated both astrocyte endfoot (30sec: P=0.0026) and fine process (30sec:
335 P=0.0029) Ca^{2+} transients around penetrators (Fig. 4C,D), and a similar trend was observed in endfeet
336 around sphincters but failed to reach significance (N=5, Suppl. Fig. 6). In a separate set of experiments
337 using c57bl/6 mice, arteriole dilation to 5sec whisker stimulation remained surprisingly unchanged in the
338 presence of D,L-AP5 (Δd/d=15.3±2.8%) from control (Δd/d=18.3±3.4%, P=0.9251, Fig. 4E). Before
339 NMDAR antagonism, vasodilation was larger during 30 sec stimulation compared to 5 sec
340 (Δd/d=27±5.1%, P=0.012, Fig. 4E), but in the presence of D,L-AP5, the late component of functional
341 hyperemia was completely blocked, as arteriole diameter returned to baseline after the initial peak
342 (Δd/d=11.8±1.6%, P=0.0214; PA=8, N=7 mice, Fig. 4E) (See figure for AUC data). These data show
343 NMDA receptors are critical for astrocyte activation and in the late phase of functional hyperemia, and
344 they argue against a NMDAR-nitric oxide link as a rapid mediator in CBF control in awake mice.
345 Epoxyeicosatrienoic acids (EETs) have been demonstrated to contribute to functional hyperemia
346 (Higashimori et al., 2010; Lecrux et al., 2011; Liu et al., 2008; Peng et al., 2002) and are primarily
347 produced by astrocytes (Alkayed et al., 1996; Peng et al., 2004). Whether blocking EETs production has

differential effects on brief vs sustained functional hyperemia has not been tested in awake mice. We measured functional hyperemia to 5sec and 30sec stimulation before and 1hr after i.p. injection of the epoxygenase inhibitor MSPPOH (30mg/kg) to c57bl/6 mice. Consistent with our proposed model, there was no difference in arteriole dilation to 5sec stimulation in the presence of MSPPOH ($\Delta d/d=10\pm1.5\%$), compared to before ($\Delta d/d=13.6\pm3\%$, $P=0.7581$) (Fig. 4F). However, 30sec stimulation was significantly attenuated by MSPPOH ($\Delta d/d=9.5\pm1.5\%$) relative to control ($\Delta d/d=20\pm3.6\%$, $P=0.0304$, PA=10, N=4 mice, Fig. 4F)(see figure for AUC data). MSPPOH yielded a similar result examining short vs long afferent stimulation-induced arteriole dilation in acute cortical brain slices (Suppl. Fig.7). These experiments show that EETs, downstream of NMDA receptor activation, are important to maintain sustained functional hyperemia.

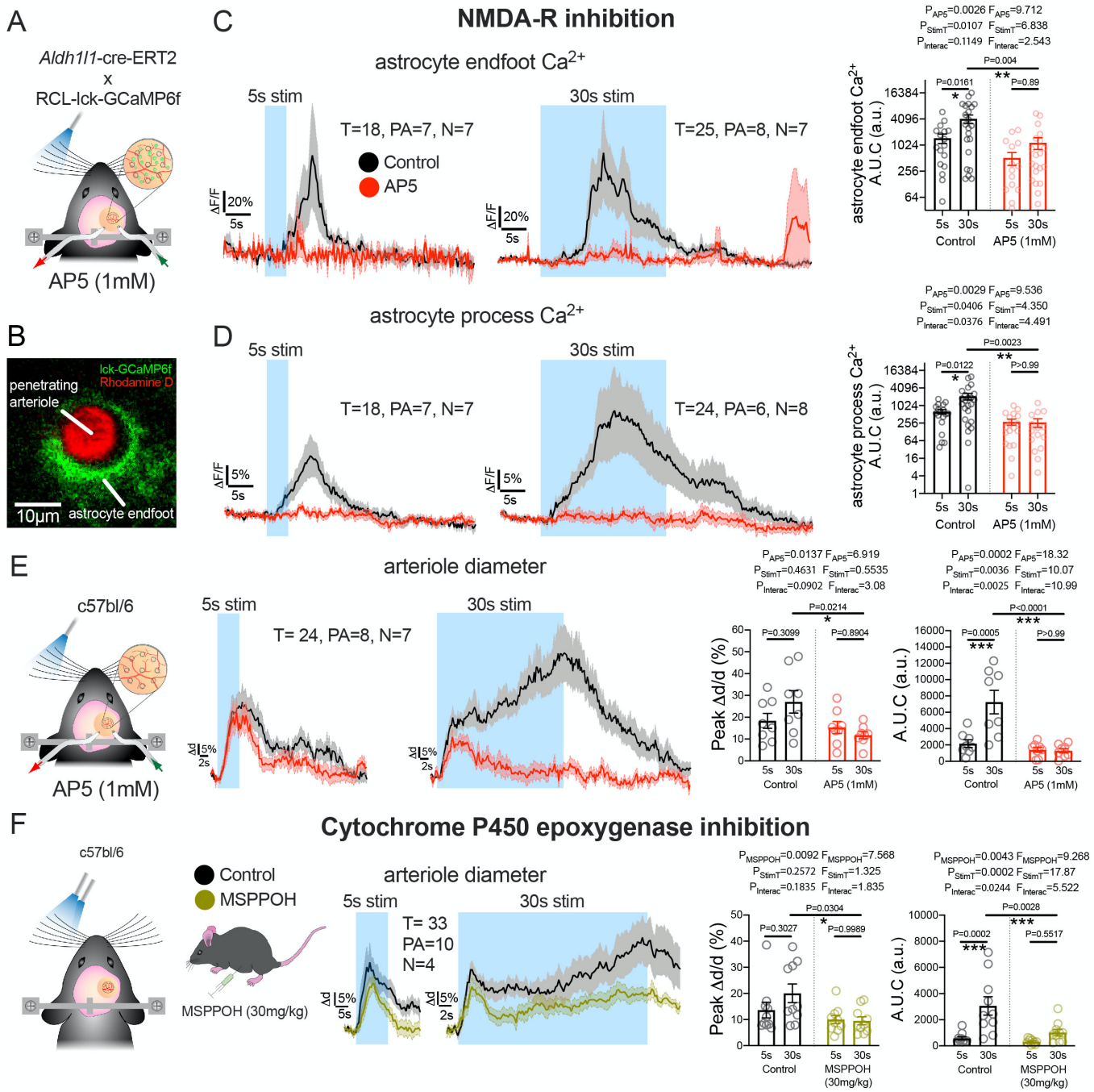
A
Aldh1l1-cre-ERT2
x
RCL-lck-GCaMP6f
AP5 (1mM)
B
lck-GCaMP6f
Rhodamine D
penetrating arteriole
10µm
astrocyte endfoot
C
NMDA-R inhibition
astrocyte endfoot Ca2+
5s stim
30s stim
T=18, PA=7, N=7
T=25, PA=8, N=7
Control
AP5
ΔF/F
20%
5s
P_AP5=0.0026 F_AP5=9.712
P_StimT=0.0107 F_StimT=6.838
P_Interac=0.1149 F_Interac=2.543
P=0.004
P=0.0161
P=0.89
astrocyte endfoot Ca2+ A.U.C (a.u.)
5s 30s 5s 30s
Control AP5 (1mM)
D
astrocyte process Ca2+
T=18, PA=7, N=7
T=24, PA=6, N=8
5%
P_AP5=0.0029 F_AP5=9.536
P_StimT=0.0406 F_StimT=4.350
P_Interac=0.0376 F_Interac=4.491
P=0.0023
P=0.0122
P>0.99
astrocyte process Ca2+ A.U.C (a.u.)
E
arteriole diameter
c57bl/6
T= 24, PA=8, N=7
Δd
2s
P_AP5=0.0137 F_AP5=6.919
P_StimT=0.4631 F_StimT=0.5535
P_Interac=0.0902 F_Interac=3.08
P=0.0214
P=0.3099
P=0.8904
Peak Δd/d (%)
P_AP5=0.0002 F_AP5=18.32
P_StimT=0.0036 F_StimT=10.07
P_Interac=0.0025 F_Interac=10.99
P<0.0001
P=0.0005
P>0.99
A.U.C (a.u.)
F
Cytochrome P450 epoxygenase inhibition
c57bl/6
Control
MSPPOH
MSPPOH (30mg/kg)
arteriole diameter
T= 33
PA=10
N=4
P_MSPPOH=0.0092 F_MSPPOH=7.568
P_StimT=0.2572 F_StimT=1.325
P_Interac=0.1835 F_Interac=1.835
P=0.0304
P=0.3027
P=0.9989
P_MSPPOH=0.0043 F_MSPPOH=9.268
P_StimT=0.0002 F_StimT=17.87
P_Interac=0.0244 F_Interac=5.522
P=0.0028
P=0.0002
P=0.5517
MSPPOH (30mg/kg)

Figure 4. NMDA receptors and epoxyeicosatrienoic acids explain astrocyte-mediated amplification of sustained functional hyperemia

A) Cartoon of awake 2-photon imaging experiment with sensory stimulation and perforated window for AP5 superfusion in Aldh1l1-CreERT2 x RCL-lck-GCaMP6f mice.
B) 2-photon image of a penetrating arteriole (red) and surrounding astrocyte expressing membrane targeted lck-GCaMP6f.
C) *Left*: Average time series trace data of astrocyte endfoot Ca^{2+} in pre-drug control (black) and in the presence of AP5 (red) surrounding a penetrating arteriole in response to 5sec and 30sec whisker stimulation. *Right*: summary data of AUC.
D) Same as for *C* but for arbor astrocyte Ca^{2+}.
E) *Left*: Cartoon of a C57Bl/6 mouse with whisker puffer and perforated cranial window for superfusion of AP5. *Middle*: Average time series traces of penetrating arteriole diameter in pre drug control (black) or in the presence of AP5 (red), in response to 5sec or 30sec whisker stimulation. *Right*: summary data of peak vasodilation and AUC.
F) Same as *E* but with sealed window and for i.p. delivery of the epoxygenase inhibitor MSPPOH (green); pre-drug control (black).

411 ## Discussion

412 By selectively attenuating or augmenting astrocyte Ca^{2+} signaling, we provide strong evidence in awake
413 mice that astrocyte Ca^{2+} does not initiate or mediate functional hyperemia when neuronal activation is
414 brief (<5s), but it is essential to amplify hyperemia when neuronal activation is prolonged. These results
415 are consistent with a large body of literature showing delayed elevations in astrocyte Ca^{2+} when neural
416 activity increases, as well as delayed increases in astrocyte metabolism (Kasischke et al., 2004). Our
417 data show that the fully awake animal is necessary to observe sufficiency effects on arteriole diameter
418 driven by astrocyte Gq (Bonder and McCarthy, 2014), and reopen the possibility of IP3R2 playing some
419 role in CBF regulation in the awake state. That selectively driving the astrocyte Gq pathway augmented
420 only sustained functional hyperemia, which is impaired in a number of neurological conditions (Weber et
421 al., 2005)(Rombouts et al., 2005)(Rombouts et al., 2007)(Pineiro et al., 2002), suggests a potential
422 therapeutic target to improve brain blood flow in these states.

423 Our *ex vivo* BAPTA and *in vivo* CalEx data indicate that fast astrocyte Ca^{2+} signals that precede
424 vasodilation (Lind et al., 2018)(Stobart et al., 2018) are not involved in the initiation or first dilation peak of
425 functional hyperemia. These same data argue against fast acting astrocyte Ca^{2+} at the capillary, pre-
426 capillary or sphincter level (Grubb et al., 2020; Hall et al., 2014; Khennouf et al., 2018) driving a rapid
427 conduction-mediated dilation to upstream arterioles (Longden et al., 2017; Tian et al., 2010). This is
428 because both astrocyte CalEx *in vivo* and astrocyte BAPTA *ex vivo* reached these vascular
429 compartments. While indirect effects of astrocyte Ca^{2+} clamp on neural activity could explain the decrease
430 in sustained functional hyperemia (Adamsky et al., 2018)(Poskanzer and Yuste, 2016), that 5sec evoked
431 vasodilation was unaffected both *in vivo* and *ex vivo* argues against general changes to neural activity
432 necessary for CBF control. Furthermore, we found no impact of astrocyte Ca^{2+} clamp on evoked neural
433 Ca^{2+} to long stimulation in brain slices, despite reduced vasodilation.

434 In sum, these data 1) help clarify the literature on the role of astrocytes in functional hyperemia –
435 a phenomenon that is fundamental to fueling the brain; 2) provide important insights into neuro-glio-
436 metabolic coupling in heath and uncoupling in disease and 3) improve our understanding and
437 interpretation of fMRI data which routinely employs stimulations or tasks of long duration.
438
439
440

Materials and methods

Animals: All animal procedures were performed in accordance with guidelines approved by the Animal Care and Use committee of the University of Calgary (protocols AC15-0133 and AC15-0053). Experiments were performed on male P22-60 c57bl/6 mice (N=35: 5 Rhod2; 8 tdT; 8 CalEx; 4 MSPPOH; 7 AP5; 3 thinned skull), transgenic *Aldh1l1*-Cre/ERT2 x RCL-GCaMP6s (Ai96)(N=9), *Aldh1l1*-Cre/ERT2 x R26-Lck-GCaMP6f (N=9), *PDGFRß*-Cre x RCL-GCaMP6s (N=11), *Aldh1l1*-Cre/ERT2 x CAG-LSL-Gq-DREADD (N=6). For the use of the Ai96 conditional line, three consecutive tamoxifen injections were administered (100 mg/kg, 10 mg/mL corn oil stock, Sigma, St. Louise MO USA) between the age of P19 to P45 and the awake imaging protocol followed at least 2 weeks later. The other ERT2 expressing mice received 4-hydroxy-tamoxifen for 2 consecutive days between P2-4 (16 mg/kg, 4mg/ml corn oil + 12 v/v (%) absolute ethanol) i.p. in a volume of 20µl.

Two-photon imaging: Two custom-built two-photon laser-scanning microscopes were used, one of which was optimized for acute brain slices and patch-clamp electrophysiology (Rosenegger et al., 2014) and another that was designed for awake *in vivo* experiments (Tran et al., 2018). Both microscopes were supplied by the same Ti:Sapph laser (Coherent Ultra II, 4 W average power, 670–1080nm, ~80MHz) and equipped with the following parts: objectives (Zeiss 40x NA 1.0, Nikon 16x NA 0.8), a green bandpass emission filter (525–40nm) and an orange/red bandpass emission filter (605–70nm) coupled to photomultiplier tubes (GaAsP Hamamatsu). The open source scanning microscope software ScanImage (version 3.81, HHMI/Janelia Farms) running in Matlab (Pologruto et al., 2003) was used for image acquisition. During acute brain slice experiments, we acquired time-series images at 0.98 Hz using bidirectional scanning of a 512 x 512 pixel-size area with 850nm laser impulses in a single focal plane visualizing fluorescent Ca^{2+} indicator-labeled cells and the center of a penetrating arteriole lumen in a depth of 40-120µm. For stimulation experiments, the Ti:Sapph was tuned to 850nm to excite Rhod-2/AM and FITC dextran fluorescent indicators. Filling of the astrocyte network with Alexa-488 was imaged at 780nm. *In vivo* experiments using Rhod-2/AM and/or FITC dextran were imaged at 850nm, at a standard 4 Hz imaging frequency, recording fluorescent signals in the top 300µm of the sensory cortex. GCaMP6 signals were imaged at 920nm, mCitrine at 980nm.

469

470 **Acute brain slice preparation:** We used Sprague-Dawley rats (p21-33) to prepare acute coronal slices of
471 the sensory-motor cortex. Rats were anesthetized with isoflurane (5% induction, 2% maintenance). Two
472 min after a fluorescent dye injection in the tail vein, animals were decapitated and their brains were quickly
473 extracted and submerged into an ice-cold slicing solution (composition in mM: 119.9 N- methyl D-
474 glucamine, 2.5 KCl, 25 $NaHCO_3$, 1.0 $CaCl_2$-$2H_2O$, 6.9 $MgCl_2$- $6H_2O$, 1.4 NaH_2PO_4-H_2O, and 20 glucose),
475 continuously bubbled with carbogen (95% O_2, 5% CO_2) for 2 min. We cut 400μm thick coronal slices with
476 a vibratome (Leica VT 1200S) and placed them to recover for 45min on a fine mesh in artificial cerebrospinal
477 fluid continuously bubbled in carbogen at 34°C. ACSF contained the following (in mM): 126 NaCl, 2.5 KCl,
478 25 $NaHCO_3$, 1.3 $CaCl_2$, 1.2 $MgCl_2$, 1.25 NaH_2PO_4, and 10 glucose.
479 The aCSF was bubbled with a gas mixture containing 30% O_2, 5% CO_2 and 65% N_2 following the
480 recovery for the dye loading period and during imaging experiments in order to enhance vascular dilation
481 responses as described previously (Institoris et al., 2015). We performed imaging at room temperature
482 (22°C) and the imaging bath was perfused with aCSF at 2ml/min by a sealed, gas pressure driven system.
483 The superfused aCSF was supplemented with the arteriole pre-constrictor U46619 (125nM) starting at least
484 30 min prior to each experiment to allow for the vessels to develop a steady tone. Drugs were infused into
485 the main superfusion ACSF line (moving at 2mL/min) through a side line driven by a syringe pump at a rate
486 of 0.2mL/min at ten-fold of the desired concentration to achieve the intended final concentration in the bath.
487

488 **Dye loading:** We labelled penetrating arterioles with Fluorescein Isothiocyanate (FITC) dextran (2000 KDa,
489 Sigma Aldrich) via a tail vein injection (15mg dissolved in 300μl lactated Ringer's solution (5%)) under
490 anesthesia immediately before slicing. Following slice recovery, slices were bulk loaded in Rhodamine-2
491 Acetoxymethyl Ester (Rhod-2/AM)(15μM, dissolved in 0.2% DMSO; 0.006% Pluronic Acid; 0.0002%
492 Cremophore EL) in 3mL of aCSF while bubbled with a 30% O_2-containing gas mixture (see above) in a
493 small incubation well for 45min at 33°C. In acute slice experiments astrocytes were identified by a brighter
494 baseline dye fluorescence than neurons due to their preferential Rhod-2/AM uptake and by the presence
495 of endfeet on vasculature.
496

497

498 **Materials:**

499 FITC-dextran (2000KDa), rhodamine B isothiocyanate-dextran (Rhodamine-dextran, 70KDa),
500 Chremophore® EL, DMSO were obtained from Sigma Aldrich. D-(-)-2-Amino-5-phosphonopentanoic acid
501 (AP5) and Compound 21 dihydrochloride was purchased from Hello Bio Inc. (Princeton, NJ). U46619 and
502 N-(methylsulfonyl)-2-(2-propynyloxy)-benzenehexanamide (MSPPOH) were ordered from Cayman
503 Chemicals. BAPTA-tetrapotassium and Alexa 488 hydrazide were obtained from Invitrogen, isoflurane from
504 Fresenius Kabi Canada Ltd., Pluronic F127 and Rhod-2 AM from Biotium, buprenorphine from Champion
505 Alstoe Animal Health, and enrofloxacin from Bayer. AAV2/5.GFaABC$_1$D-GCamP6f was ordered from Penn
506 Vector Core, PA, USA and AAV2/5.GFaABC$_1$D-tdTomato from Addgene, MA, USA.

507

508 **Electrical stimulation:** The activation of afferent fibres was elicited by electric stimulation using an
509 assembly of a Grass S88X stimulator, a voltage isolation unit and a concentric bipolar electrode (FHC). We
510 softly positioned the electrode onto the surface of the slice by a micro-manipulator ~250µm lateral to the
511 penetrating arteriole. The tissue was stimulated for 5sec or 30sec with a theta burst pattern (trains of 1 ms
512 mono-polar pulses at 100Hz for 50ms, repeated at 4Hz) using a 0.1V higher intensity than the threshold of
513 astrocyte endfoot activation (1.1-1.3V). This threshold was determined by gradually ramping the voltage
514 (+0.1V) of a low frequency (20Hz) 5sec stimulation until an endfoot Ca^{2+} transient was observed. For some
515 experiments (see Suppl. Fig. 7), we employed a 20Hz stimulation for 5sec with low intensity that did not
516 activate astrocyte endfeet and subsequent 30sec stimulations used the same voltage.

517

518 **Astrocyte patch clamping experiments:** Patching experiments were conducted similar to our previous
519 publication (Rosenegger et al., 2015). Before the patching process, slices were electrically stimulated for 5
520 or 30sec with a theta burst pattern. Next, astrocytes were selected in the 30-70 µm proximity of an arteriole
521 at a 30-60 µm depth, typically above the imaging plane of the arteriole (Suppl. Fig. 4A). A 3-5 MΩ resistance
522 glass electrode formed a GΩ seal on the cell body membrane and when whole cell configuration was
523 achieved astrocytes were filled with an internal solution containing the fluorescent dye Alexa-488 (100-200
524 µM) to visualize diffusion, and the following substances (in mM): 8 KCl, 8 Na- gluconate, 2 $MgCl_2$, 10

525 HEPES, 4.38 $CaCl_2$, 4 K-ATP, and 0.3 Na-GTP, 10 K-BAPTA (1,2-bis(o-aminophenoxy) ethane-N,N,N',N'-
526 tetraacetic acid) with 96 K-gluconate. Osmolality was adjusted to ~285 mOsm, pH was corrected with KOH
527 to 7.2. We voltage clamped astrocytes at -80 mV and confirmed the cell type by a low input resistance (10-
528 20 MΩ) and dye filling of the endfeet circumventing a large section of the arteriole (Suppl. Fig. 4A,B).
529 Importantly, dye filling of the endfeet with a clamping solution of 100nM Ca^{2+} did not change arteriole tone
530 *per se* (see Suppl. Fig. 5). We allowed 15-30 min for the internal solution to washout from the tissue and
531 for the arteriole tone to return to baseline. Then we repeated the electric stimulation to compare to the first
532 response.
533
534 **Awake *in vivo* two-photon imaging:** Male mice were used according to the protocol previously developed
535 by our laboratory (Tran et al., 2018). Briefly, on day 1, under isoflurane anesthesia (induction 4%,
536 maintenance 1.5-2%), pain control (buprenorphine 0.05mg/kg) and antibiotic premedication (enrofloxacin
537 2.5 mg/kg), a light (0.5 g) metal headbar was glued on the occipital bone under aseptic conditions with a
538 three component dental glue (C&B Metabond, Parkell Inc, NY, USA) and dental cement (OrthoJet Acrylic
539 Resin, Land Dental MFG. CO., Inc., IL, USA). After a recovery period of 24hr, the mice were trained on
540 days 2 and 3 to habituate to imaging and air puff stimulation to the whiskers while head fixed but free to
541 move on a passive, air supported spherical Styrofoam ball in a light tight environment (Fig. 1A). After 15
542 min of rest, intermittent air puffs (125ms at 4Hz for 5s)(50 psi, Picospritzer III, General Valve) were delivered
543 to the contralateral whiskers 15 times every 10s, 15s, 30s and 60s, respectively on day 2 and 3. On day 4,
544 a craniotomy was performed over the barrel cortex. Bone and dura were gently removed. For N=6 c57bl/6
545 and for *Aldh1l1*-Cre/ERT2 x CAG-LSL-Gq-DREADD mice, Rhod-2 AM (15μM) in aCSF was incubated on
546 the brain surface for 45 min. Next, the window was fully sealed with a coverslip. In experiments where
547 astrocyte endfeet were labelled with a red fluorescent dye, 0.2mL 5% FITC dextran solution was injected
548 into the tail vein immediately before imaging, whereas Rhodamine-dextran (0.2mL, 2.3%) was injected
549 when astrocytes expressed GCaMP6. The animals were transferred to the imaging rig, where imaging
550 started ~30min after the animals awoke. Behavior was continuously monitored by a camera detecting the
551 light of an infrared LED and was recorded during imaging. A 16x or a 40x water-immersion objective was
552 positioned square to the surface of the window. Imaging was performed at 4Hz or at 0.5Hz when drug

553 application was recorded. Rhod-2 AM only loaded astrocytes in mice *in vivo* as neuronal compartments
554 were neither labeled at rest nor appeared in response to stimulation (Tran et al., 2018).
555
556 **AAV CalEx injection:** P22-35 male c57bl/6 mice (N=8), under isoflurane anesthesia and aseptic
557 conditions, received a vertical nano-injection into the barrel cortex (bregma 3mm lat., 1mm post.) with an
558 astrocytic viral cocktail containing the CalEx encoding construct AAV2/5.GfaABC$_1$D mCherry-hPMCA2w/b
559 (1.2 x 10^{13} gc/ml) + AAV2/5.GfaABC$_1$D GCaMP6f (3 x 10^{12} gc/ml, Addgene) mixed in a 3:1 ratio in a volume
560 of 414nL, delivered by a Nanoject II (Drummond Scientific, Broomall, PA, USA) . Control mice (N=8)
561 received the same titer and volume of AAV2/5.GfaABC$_1$D tdTomato (1.2 x 10^{13} gc/ml) + AAV2/5.GfaABC$_1$D
562 GCaMP6f (3 x 10^{12} gc/ml). Head bar installation, training and imaging took place 4-6 weeks later, because
563 this is sufficient time to achieve functionally effective CalEx expression (Yu et al., 2018).
564
565 **Immunohistochemistry:** Slices were collected from control and CalEx mice at the end of the *in vivo*
566 experiments and post-fixed in 4% paraformaldehyde overnight and then cryoprotected in 30% sucrose for
567 another 24hr. Sections were cut on a cryostat to 14µm and mounted onto chrom alum slides. The slides
568 were first washed in PBS (phosphate buffered saline) for 30min, followed by 2 x 10min washes in PBS. A
569 blocking agent (3% bovine serum albumin (BSA), 0.3% Triton X in PBS) was applied for 1 hour and placed
570 in a humidor. For mCherry labeling, Anti-RFP (rabbit) primary antibody (1:100: Rockland) was diluted in
571 blocking agent and incubated for 24hr in a humidor at room temperature. After primary antibody incubation,
572 sections were washed three times with PBS and then incubated for 2hr with Alexa Fluor 594 (1:100:
573 Molecular Probes) diluted in blocking agent and placed in the humidor for 24hr. Sections were then washed
574 again three times with PBS before mounting coverslips with Vectashield (Vector Labs) and read on a
575 confocal fluorescence microscope (Leica TCS SP8, Leica Microsystems).
576
577 **Functional hyperemia:** Each imaging session started by confirming Rhod-2/AM, GCaMP6 or Gq
578 DREADD-linked mCitrine expression and identifying the vascular network by z-stack imaging to a depth of
579 ~300µm with a 16x objective. Pial arterioles were distinguished from veins by spontaneous vasomotion and
580 by positive responses to contralateral whisker air puff. Penetrating arteriole branches of the pial arteries

581 were tracked and imaged at a depth of 50-250μm with a 40x objective. Air puff was delivered through 2
582 glass capillary tubes positioned to deflect as many whiskers as possible without blowing air on the face
583 (Fig. 1A). A 10sec baseline period was recorded after which an intermittent 5sec or 30sec 4Hz (125ms
584 pulses) air puff (50psi) was employed. Stimulation was repeated 3-6 times and averaged for each arteriole.
585 When Rhodamine signal was not well visible at 920nm, whisker stimulations were repeated at 850nm.
586
587 **Data processing and statistical analysis:** Ca^{2+} signals were analyzed in ImageJ (NIH) and calculated in
588 Prism software (GraphPad Inc., La Jolla, CA) as follows: $\Delta F/F=((F1- F0)/F0) \times 100$, where F is fluorescence,
589 1 is at any given time point, and 0 is an average baseline value of 60sec *ex vivo* or 2sec *in vivo* pre stimulus.
590 Ca^{2+} responses in brain slices were obtained by selecting a region of interest (ROI) and running the
591 'intensity vs. time monitor' plugin over the following compartments: (1) neuropil was outlined as an acellular
592 region next to the region of vasodilation on the side closer to the stimulating electrode, (2) neuron soma
593 responses were the average of 5 neuronal cell bodies visible in the imaging plane closest to the arteriole,
594 (3) astrocyte soma signal was the average of 1-3 cells closest to the arteriole, (4) astrocyte endfoot was
595 chosen as a clearly visible continuous structure adjacent to the area of vasodilation. The same ROIs were
596 used after patching *in vitro* or after drug administration *in vivo*. Astrocyte GCaMP6 signals of endfeet and
597 processes in all experiments were outlined by including regions around the arteriole were an increase in
598 the fluorescent signal was visible after stimulation onset.
599 In the absence of stimulus-evoked fluorescence changes, areas of basal GCaMP6 fluorescence
600 was selected. Ca^{2+} signals are labeled as $\Delta F/F_c$ in control conditions, $\Delta F/F_{BAPTA}$ after BAPTA loading. Pre-
601 processing of intraluminal dye recordings included xy-motion correction, median filter (0.5-2 pixel radius)
602 and Gaussian filter (1-4 pixel radius) performed by ImageJ plugins. Intraluminal area was selected by
603 intensity thresholding and quantified using the 'Analyze particles' function of ImageJ.
604 Arteriole diameter changes were quantified as the relative change in the area of intraluminal dye
605 along the longitudinal section (in slice) or calculated from the cross-sectional area (*in vivo*) of the vascular
606 lumen, assuming a circular shape, as follows: diameter = $2x \sqrt{(area/\pi)}$. Stimulation-evoked vasodilation
607 was first calculated as Δ diameter (Δd) = $(diameter_1-diameter_0)/diameter_0) \times 100$ (%), where $diameter_1$ is
608 the diameter of the vascular lumen at any time point and $diameter_0$ is the average baseline vascular lumen

609 diameter 2sec prior to stimulation onset. Response latency was determined as the time from stimulation
610 onset until 2 consecutive values exceeded 3 standard deviations of the 2sec baseline.
611 All peak responses during topical C21 application (first 10min from Ca^{2+} increase onset) were
612 compared to the peak value of the 500sec baseline period (see Fig. 3C). AUC values were calculated from
613 Δd traces as the summary of all positive peaks over the baseline value from stimulation onset until values
614 are displayed in the figures.
615 Statistical analyses were performed on averaged trials of PA responses and on Ca^{2+} responses of
616 individual stimulation trials *in vivo*. Normality was tested with Shapiro-Wilk test. Normally distributed data
617 were evaluated with a paired or unpaired Student's t-test, and non-normally distributed with Mann-Whitney
618 or Wilcoxon test. The non-parametric Friedman test and Dunn's multiple comparison test was applied to
619 compare *in vivo* peak diameter changes on stimulation length (1- 5- 30sec). Repeated-measures two-way
620 ANOVA was run to compare the effects of stimulation length (5sec vs 30sec as within subject variables)
621 and external manipulations (CalEx, or drug treatments), followed by Tukey's post hoc test for pairwise
622 comparison. Baseline arteriole diameter (intravascular area) changes were analyzed with the two-tailed
623 non-parametric Wilcoxon test in Prism. Data are expressed as mean ± standard error of the mean (SEM).
624
625 **Amazon Mechanical Turk analysis:**
626 Arteriole diameter changes of the CalEx experiments were analyzed by manual outlining of the FITC
627 dextran loaded vascular lumen frame by frame in an outsourced and randomized fashion, using Amazon
628 Mechanical Turk (Suppl. Fig. 8). It is an online crowdsourcing website, through which remotely located
629 "crowd-workers" are hired to perform a discrete on-demand task. A custom-made GUI facilitated the manual
630 outlining of the vascular cross-section over the course of the recording. An annotation task consisted of
631 adjusting a polygonal shape with a fixed number of vertices on the top of the vessel. To keep annotations
632 consistent, crowd-workers could inspect the time evolution of the vessel and their annotations by freely
633 scrolling through the time-lapse images. Annotation tasks were randomly assigned to 10 different crowd-
634 workers, blind to the experiment (example task: https://codepen.io/leonardomt/full/jOEvPvY). Each stack
635 of images was then visually examined and accepted or rejected based on whether the instructions were
636 followed or not, i.e., if outlines were not consistently labeled over time or if there was a clear mismatch in

637 the outlines with respect to the brain vessel. The area of each polygonal shape was then calculated and
638 normalized (Suppl. Fig. 8)
639

640 **Acknowledgement**

641 This work was supported by the Canadian Institutes of Health Research. G.R.G. was supported by Canada
642 Research Chairs. We thank Dr. David Rosenegger for preliminary patch experiments. We thank Dr. Ciaran
643 Murphy-Royal for his valuable scientific comments. We thank Dr. Vincent Ebacher and the HBI advanced
644 microscopy platform for the confocal microscope images and the CSM Optogenetics Facility for hosting the
645 web services for crowdsourced annotations. We are grateful for Dr. Frank Visser for transgenic mouse
646 sample genotyping. We thank the developers and distributers of ScanImage open-source control and
647 acquisition software for two-photon laser-scanning microscopy.
648

649 **Author's contribution**

650 A.I. designed and performed experiments, analyzed results and wrote the paper. M.V. and G.P. performed
651 experiments and analyzed results, C.H.T. performed experiments, X.Y. and B.S.K. designed CalEx virus
652 construct, C.B. did immunohistochemistry, L.M. designed platform for crowdsourcing annotations with
653 Amazon Mechanical Turk and supervised analysis. G.R.G. designed experiments and wrote the paper.
654

655 **Declaration of interest**

656 The authors declare no competing interests.
657

658 **Data availability**

659 The data that support the findings of this study are available from the corresponding author upon
660 reasonable request.
661
662

Citations

Adamsky, A., Kol, A., Kreisel, T., Doron, A., Ozeri-Engelhard, N., Melcer, T., Refaeli, R., Horn, H., Regev, L., Groysman, M., et al. (2018). Astrocytic Activation Generates De Novo Neuronal Potentiation and Memory Enhancement. Cell *174*, 59-71.e14.

Alkayed, N.J., Narayanan, J., Gebremedhin, D., Medhora, M., Roman, R.J., and Harder, D.R. (1996). Molecular characterization of an arachidonic acid epoxygenase in rat brain astrocytes. Stroke *27*, 971–979.

Bonder, D.E., and McCarthy, K.D. (2014). Astrocytic Gq-GPCR-linked IP3R-dependent Ca2+ signaling does not mediate neurovascular coupling in mouse visual cortex in vivo. J. Neurosci. *34*, 13139–13150.

Busija, D.W., Bari, F., Domoki, F., and Louis, T. (2007). Mechanisms Involved in the Cerebrovascular Dilator Effects of N-methyl-D-aspartate in Cerebral Cortex. Brain Res Rev *56*, 89–100.

Cauli, B., and Hamel, E. (2010). Revisiting the role of neurons in neurovascular coupling. Front Neuroenergetics *2*, 9.

Chow, B.W., Nuñez, V., Kaplan, L., Granger, A.J., Bistrong, K., Zucker, H.L., Kumar, P., Sabatini, B.L., and Gu, C. (2020). Caveolae in CNS arterioles mediate neurovascular coupling. Nature *579*, 106–110.

Drew, P.J., Shih, A.Y., and Kleinfeld, D. (2011). Fluctuating and sensory-induced vasodynamics in rodent cortex extend arteriole capacity. Proc Natl Acad Sci U S A *108*, 8473–8478.

Grubb, S., Cai, C., Hald, B.O., Khennouf, L., Murmu, R.P., Jensen, A.G.K., Fordsmann, J., Zambach, S., and Lauritzen, M. (2020). Precapillary sphincters maintain perfusion in the cerebral cortex. Nat Commun *11*, 395.

Gu, X., Chen, W., Volkow, N.D., Koretsky, A.P., Du, C., and Pan, Y. (2018). Synchronized Astrocytic Ca2+ Responses in Neurovascular Coupling during Somatosensory Stimulation and for the Resting State. Cell Rep *23*, 3878–3890.

Hall, C.N., Reynell, C., Gesslein, B., Hamilton, N.B., Mishra, A., Sutherland, B.A., O'Farrell, F.M., Buchan, A.M., Lauritzen, M., and Attwell, D. (2014). Capillary pericytes regulate cerebral blood flow in health and disease. Nature *508*, 55–60.

He, Y., Wang, M., Chen, X., Pohmann, R., Polimeni, J.R., Scheffler, K., Rosen, B.R., Kleinfeld, D., and Yu, X. (2018). Ultra-Slow Single-Vessel BOLD and CBV-Based fMRI Spatiotemporal Dynamics and Their Correlation with Neuronal Intracellular Calcium Signals. Neuron *97*, 925-939.e5.

Henneberger, C., Papouin, T., Oliet, S.H.R., and Rusakov, D.A. (2010). Long-term potentiation depends on release of D-serine from astrocytes. Nature *463*, 232–236.

Higashimori, H., Blanco, V.M., Tuniki, V.R., Falck, J.R., and Filosa, J.A. (2010). Role of epoxyeicosatrienoic acids as autocrine metabolites in glutamate-mediated K+ signaling in perivascular astrocytes. Am J Physiol Cell Physiol *299*, C1068-1078.

Hill, R.A., Tong, L., Yuan, P., Murikinati, S., Gupta, S., and Grutzendler, J. (2015). Regional Blood Flow in the Normal and Ischemic Brain Is Controlled by Arteriolar Smooth Muscle Cell Contractility and Not by Capillary Pericytes. Neuron *87*, 95–110.

Hogan-Cann, A.D., Lu, P., and Anderson, C.M. (2019). Endothelial NMDA receptors mediate activity-dependent brain hemodynamic responses in mice. Proc Natl Acad Sci U S A *116*, 10229–10231.

Hosford, P.S., and Gourine, A.V. (2019). What is the key mediator of the neurovascular coupling response? Neurosci Biobehav Rev *96*, 174–181.

Howarth, C. (2014). The contribution of astrocytes to the regulation of cerebral blood flow. Front Neurosci *8*, 103.

Howarth, C., Gleeson, P., and Attwell, D. (2012). Updated energy budgets for neural computation in the neocortex and cerebellum. J. Cereb. Blood Flow Metab. *32*, 1222–1232.

Institoris, Á., Rosenegger, D.G., and Gordon, G.R. (2015). Arteriole dilation to synaptic activation that is sub-threshold to astrocyte endfoot Ca2+ transients. J. Cereb. Blood Flow Metab. *35*, 1411–1415.

Jego, P., Pacheco-Torres, J., Araque, A., and Canals, S. (2014). Functional MRI in Mice Lacking IP3-Dependent Calcium Signaling in Astrocytes: Journal of Cerebral Blood Flow & Metabolism.

Kahn, I., Desai, M., Knoblich, U., Bernstein, J., Henninger, M., Graybiel, A.M., Boyden, E.S., Buckner, R.L., and Moore, C.I. (2011). Characterization of the Functional MRI Response Temporal Linearity via Optical Control of Neocortical Pyramidal Neurons. J. Neurosci. *31*, 15086–15091.

Kasischke, K.A., Vishwasrao, H.D., Fisher, P.J., Zipfel, W.R., and Webb, W.W. (2004). Neural Activity Triggers Neuronal Oxidative Metabolism Followed by Astrocytic Glycolysis. Science *305*, 99–103.

Khennouf, L., Gesslein, B., Brazhe, A., Octeau, J.C., Kutuzov, N., Khakh, B.S., and Lauritzen, M. (2018). Active role of capillary pericytes during stimulation-induced activity and spreading depolarization. Brain *141*, 2032–2046.

Lacroix, A., Toussay, X., Anenberg, E., Lecrux, C., Ferreirós, N., Karagiannis, A., Plaisier, F., Chausson, P., Jarlier, F., Burgess, S.A., et al. (2015). COX-2-Derived Prostaglandin E2 Produced by Pyramidal Neurons Contributes to Neurovascular Coupling in the Rodent Cerebral Cortex. J. Neurosci. *35*, 11791–11810.

Lecrux, C., Toussay, X., Kocharyan, A., Fernandes, P., Neupane, S., Lévesque, M., Plaisier, F., Shmuel, A., Cauli, B., and Hamel, E. (2011). Pyramidal neurons are “neurogenic hubs” in the neurovascular coupling response to whisker stimulation. J. Neurosci. *31*, 9836–9847.

Lee, J.H., Durand, R., Gradinaru, V., Zhang, F., Goshen, I., Kim, D.-S., Fenno, L.E., Ramakrishnan, C., and Deisseroth, K. (2010). Global and local fMRI signals driven by neurons defined optogenetically by type and wiring. Nature *465*, 788–792.

Lind, B.L., Jessen, S.B., Lønstrup, M., Joséphine, C., Bonvento, G., and Lauritzen, M. (2018). Fast Ca2+ responses in astrocyte end-feet and neurovascular coupling in mice. Glia *66*, 348–358.

Liu, X., Li, C., Falck, J.R., Roman, R.J., Harder, D.R., and Koehler, R.C. (2008). Interaction of nitric oxide, 20-HETE, and EETs during functional hyperemia in whisker barrel cortex. Am. J. Physiol. Heart Circ. Physiol. *295*, H619-631.

Logothetis, N.K., Pauls, J., Augath, M., Trinath, T., and Oeltermann, A. (2001). Neurophysiological investigation of the basis of the fMRI signal. Nature *412*, 150–157.

Longden, T.A., Dabertrand, F., Koide, M., Gonzales, A.L., Tykocki, N.R., Brayden, J.E., Hill-Eubanks, D., and Nelson, M.T. (2017). Capillary K+-sensing initiates retrograde hyperpolarization to increase local cerebral blood flow. Nat. Neurosci. *20*, 717–726.

Masamoto, K., Unekawa, M., Watanabe, T., Toriumi, H., Takuwa, H., Kawaguchi, H., Kanno, I., Matsui, K., Tanaka, K.F., Tomita, Y., et al. (2015). Unveiling astrocytic control of cerebral blood flow with optogenetics. Sci Rep *5*.

Mateo, C., Knutsen, P.M., Tsai, P.S., Shih, A.Y., and Kleinfeld, D. (2017). Entrainment of Arteriole Vasomotor Fluctuations by Neural Activity Is a Basis of Blood-Oxygenation-Level-Dependent "Resting-State" Connectivity. Neuron *96*, 936-948.e3.

Mehina, E.M.F., Murphy-Royal, C., and Gordon, G.R. (2017). Steady-State Free Ca2+ in Astrocytes Is Decreased by Experience and Impacts Arteriole Tone. J. Neurosci. *37*, 8150–8165.

Mishra, A. (2017). Binaural blood flow control by astrocytes: listening to synapses and the vasculature. J. Physiol. (Lond.) *595*, 1885–1902.

Mishra, A., Reynolds, J.P., Chen, Y., Gourine, A.V., Rusakov, D.A., and Attwell, D. (2016). Astrocytes mediate neurovascular signaling to capillary pericytes but not to arterioles. Nat. Neurosci. *19*, 1619–1627.

Nizar, K., Uhlirova, H., Tian, P., Saisan, P.A., Cheng, Q., Reznichenko, L., Weldy, K.L., Steed, T.C., Sridhar, V.B., MacDonald, C.L., et al. (2013). In vivo stimulus-induced vasodilation occurs without IP3 receptor activation and may precede astrocytic calcium increase. J. Neurosci. *33*, 8411–8422.

Otsu, Y., Couchman, K., Lyons, D.G., Collot, M., Agarwal, A., Mallet, J.-M., Pfrieger, F.W., Bergles, D.E., and Charpak, S. (2015). Calcium dynamics in astrocyte processes during neurovascular coupling. Nat. Neurosci. *18*, 210–218.

Peng, X., Carhuapoma, J.R., Bhardwaj, A., Alkayed, N.J., Falck, J.R., Harder, D.R., Traystman, R.J., and Koehler, R.C. (2002). Suppression of cortical functional hyperemia to vibrissal stimulation in the rat by epoxygenase inhibitors. American Journal of Physiology-Heart and Circulatory Physiology *283*, H2029–H2037.

Peng, X., Zhang, C., Alkayed, N.J., Harder, D.R., and Koehler, R.C. (2004). Dependency of cortical functional hyperemia to forepaw stimulation on epoxygenase and nitric oxide synthase activities in rats. J Cereb Blood Flow Metab *24*, 509–517.

Pineiro, R., Pendlebury, S., Johansen-Berg, H., and Matthews, P.M. (2002). Altered hemodynamic responses in patients after subcortical stroke measured by functional MRI. Stroke *33*, 103–109.

Polesskaya, O., Sun, A., Salahura, G., Silva, J.N., Dewhurst, S., and Kasischke, K. (2012). Detection of Microregional Hypoxia in Mouse Cerebral Cortex by Two-photon Imaging of Endogenous NADH Fluorescence. J Vis Exp.

Pologruto, T.A., Sabatini, B.L., and Svoboda, K. (2003). ScanImage: flexible software for operating laser scanning microscopes. Biomed Eng Online *2*, 13.

Porter, J.T., and McCarthy, K.D. (1996). Hippocampal astrocytes in situ respond to glutamate released from synaptic terminals. J Neurosci *16*, 5073–5081.

Poskanzer, K.E., and Yuste, R. (2016). Astrocytes regulate cortical state switching in vivo. Proc Natl Acad Sci U S A *113*, E2675-2684.

Rombouts, S.A.R.B., Goekoop, R., Stam, C.J., Barkhof, F., and Scheltens, P. (2005). Delayed rather than decreased BOLD response as a marker for early Alzheimer's disease. Neuroimage *26*, 1078–1085.

Rombouts, S.A.R.B., Scheltens, P., Kuijer, J.P.A., and Barkhof, F. (2007). Whole brain analysis of T2* weighted baseline FMRI signal in dementia. Hum Brain Mapp *28*, 1313–1317.

780 Rosenegger, D.G., Tran, C.H.T., LeDue, J., Zhou, N., and Gordon, G.R. (2014). A high performance,
781 cost-effective, open-source microscope for scanning two-photon microscopy that is modular and readily
782 adaptable. PLoS ONE *9*, e110475.

783 Rosenegger, D.G., Tran, C.H.T., Wamsteeker Cusulin, J.I., and Gordon, G.R. (2015). Tonic Local Brain
784 Blood Flow Control by Astrocytes Independent of Phasic Neurovascular Coupling. J. Neurosci. *35*,
785 13463–13474.

786 Rungta, R.L., Chaigneau, E., Osmanski, B.-F., and Charpak, S. (2018). Vascular Compartmentalization of
787 Functional Hyperemia from the Synapse to the Pia. Neuron *99*, 362-375.e4.

788 Schulz, K., Sydekum, E., Krueppel, R., Engelbrecht, C.J., Schlegel, F., Schröter, A., Rudin, M., and
789 Helmchen, F. (2012). Simultaneous BOLD fMRI and fiber-optic calcium recording in rat neocortex. Nat
790 Methods *9*, 597–602.

791 Stobart, J.L., Ferrari, K.D., Barrett, M.J.P., Glück, C., Stobart, M.J., Zuend, M., and Weber, B. (2018).
792 Cortical Circuit Activity Evokes Rapid Astrocyte Calcium Signals on a Similar Timescale to Neurons.
793 Neuron *98*, 726-735.e4.

794 Takano, T., Tian, G.-F., Peng, W., Lou, N., Libionka, W., Han, X., and Nedergaard, M. (2006). Astrocyte-
795 mediated control of cerebral blood flow. Nat Neurosci *9*, 260–267.

796 Takata, N., Nagai, T., Ozawa, K., Oe, Y., Mikoshiba, K., and Hirase, H. (2013). Cerebral blood flow
797 modulation by Basal forebrain or whisker stimulation can occur independently of large cytosolic Ca2+
798 signaling in astrocytes. PLoS ONE *8*, e66525.

799 Takata, N., Sugiura, Y., Yoshida, K., Koizumi, M., Hiroshi, N., Honda, K., Yano, R., Komaki, Y., Matsui,
800 K., Suematsu, M., et al. (2018). Optogenetic astrocyte activation evokes BOLD fMRI response with
801 oxygen consumption without neuronal activity modulation. Glia *66*, 2013–2023.

802 Takuwa, H., Masamoto, K., Yamazaki, K., Kawaguchi, H., Ikoma, Y., Tajima, Y., Obata, T., Tomita, Y.,
803 Suzuki, N., Kanno, I., et al. (2013). Long-Term Adaptation of Cerebral Hemodynamic Response to
804 Somatosensory Stimulation during Chronic Hypoxia in Awake Mice: Journal of Cerebral Blood Flow &
805 Metabolism.

806 Thrane, A.S., Rangroo Thrane, V., Zeppenfeld, D., Lou, N., Xu, Q., Nagelhus, E.A., and Nedergaard, M.
807 (2012). General anesthesia selectively disrupts astrocyte calcium signaling in the awake mouse cortex.
808 Proc. Natl. Acad. Sci. U.S.A. *109*, 18974–18979.

809 Tian, P., Teng, I.C., May, L.D., Kurz, R., Lu, K., Scadeng, M., Hillman, E.M.C., De Crespigny, A.J.,
810 D'Arceuil, H.E., Mandeville, J.B., et al. (2010). Cortical depth-specific microvascular dilation underlies
811 laminar differences in blood oxygenation level-dependent functional MRI signal. Proc. Natl. Acad. Sci.
812 U.S.A. *107*, 15246–15251.

813 Toth, P., Tarantini, S., Davila, A., Valcarcel-Ares, M.N., Tucsek, Z., Varamini, B., Ballabh, P., Sonntag,
814 W.E., Baur, J.A., Csiszar, A., et al. (2015). Purinergic glio-endothelial coupling during neuronal activity:
815 role of P2Y1 receptors and eNOS in functional hyperemia in the mouse somatosensory cortex. Am. J.
816 Physiol. Heart Circ. Physiol. *309*, H1837-1845.

817 Tran, C.H.T., and Gordon, G.R. (2015). Astrocyte and microvascular imaging in awake animals using two-
818 photon microscopy. Microcirculation *22*, 219–227.

819 Tran, C.H.T., Peringod, G., and Gordon, G.R. (2018). Astrocytes Integrate Behavioral State and Vascular
820 Signals during Functional Hyperemia. Neuron *100*, 1133-1148.e3.

Wang, X., Lou, N., Xu, Q., Tian, G.-F., Peng, W.G., Han, X., Kang, J., Takano, T., and Nedergaard, M. (2006). Astrocytic Ca2+ signaling evoked by sensory stimulation in vivo. Nat Neurosci *9*, 816–823.

Weber, P., Lütschg, J., and Fahnenstich, H. (2005). Cerebral hemodynamic changes in response to an executive function task in children with attention-deficit hyperactivity disorder measured by near-infrared spectroscopy. J Dev Behav Pediatr *26*, 105–111.

Yu, X., Taylor, A.M.W., Nagai, J., Golshani, P., Evans, C.J., Coppola, G., and Khakh, B.S. (2018). Reducing Astrocyte Calcium Signaling In Vivo Alters Striatal Microcircuits and Causes Repetitive Behavior. Neuron *99*, 1170-1187.e9.

Zheng, K., Bard, L., Reynolds, J.P., King, C., Jensen, T.P., Gourine, A.V., and Rusakov, D.A. (2015). Time-Resolved Imaging Reveals Heterogeneous Landscapes of Nanomolar Ca(2+) in Neurons and Astroglia. Neuron *88*, 277–288.

Zonta, M., Angulo, M.C., Gobbo, S., Rosengarten, B., Hossmann, K.-A., Pozzan, T., and Carmignoto, G. (2003). Neuron-to-astrocyte signaling is central to the dynamic control of brain microcirculation. Nat Neurosci *6*, 43–50.